

**Photoemission study of pristine and Ni-doped SrTiO<sub>3</sub> thin films**

Fatima Alarab,<sup>1,2,3</sup> Karol Hricovini,<sup>1,3</sup> Berengar Leikert,<sup>4</sup> Laurent Nicolai<sup>Ⓢ</sup>,<sup>2</sup> Mauro Fanciulli<sup>Ⓢ</sup>,<sup>1,3</sup> Olivier Heckmann,<sup>1,3</sup> Christine Richter<sup>Ⓢ</sup>,<sup>1,3</sup> Lucie Prušaková,<sup>2</sup> Zdeňek Jansa,<sup>2</sup> Pavol Šutta,<sup>2</sup> Julien Rault<sup>Ⓢ</sup>,<sup>5</sup> Patrick Lefevre,<sup>5</sup> Michael Sing,<sup>4</sup>

Matthias Muntwiler<sup>Ⓢ</sup>,<sup>6</sup> Ralph Claessen<sup>Ⓢ</sup>,<sup>4</sup> and Ján Minár<sup>Ⓢ</sup><sup>2</sup>

<sup>1</sup>*LPMS, CY Cergy Paris Université, 95000 Neuville-sur-Oise, France*


<sup>2</sup>*New Technologies Research Centre, University of West Bohemia, 30614 Pilsen, Czech Republic*

<sup>3</sup>*LYDIL, CEA, Université Paris-Saclay, 91191 Gif-sur-Yvette, France*

<sup>4</sup>*Physikalisches Institut and Würzburg-Dresden Cluster of Excellence ct.qmat, Julius-Maximilians-Universität, 97074 Würzburg, Germany*

<sup>5</sup>*Synchrotron SOLEIL, Saint-Aubin, 91191 Gif-sur-Yvette, France*

<sup>6</sup>*Swiss Light Source, Paul Scherrer Institut, 5232 Villigen, Switzerland*

 (Received 11 March 2021; revised 6 September 2021; accepted 4 October 2021; published 18 October 2021)

We combined photoelectron spectroscopy with first-principles calculations to investigate electronic properties of SrTiO<sub>3</sub> doped with Ni impurities. High-quality epitaxial pristine SrTiO<sub>3</sub> and SrTiO<sub>3</sub>:Ni<sub>x</sub> films with  $x = 0.06$  and  $0.12$  were prepared by pulsed laser deposition. Electronic band structure calculations for the ground state, as well as one-step model photoemission calculations, which were obtained by means of the Korringa-Kohn-Rostoker Green's function method, predict the formation of localized  $3d$ -impurity bands in the band gap of SrTiO<sub>3</sub> close to the valence band maxima. The measured valence bands at the resonance Ni  $2p$  excitation and band dispersion confirm these findings.

DOI: [10.1103/PhysRevB.104.165129](https://doi.org/10.1103/PhysRevB.104.165129)

**I. INTRODUCTION**

Transition metal oxides with perovskite structure are receiving a large amount of attention from scientists because of their outstanding properties, such as high-temperature superconductivity [1–3], large negative magnetoresistance [4], multiferroicity [5], and the formation of a two-dimensional electron gas (2DEG) at oxide surfaces and interfaces [6–9].

They have been studied in recent years for their use as flexible and adaptable materials for several technological applications, especially for harvesting solar light and for photocatalysis [10–15]. The prototypical perovskite-structured complex oxide strontium titanate (STO) is active only under UV light and remains transparent for visible light due to its wide band gap, which is about 3.25 eV at room temperature [16]. This inactivity in the visible light calls for solving the problem by band-gap tuning. In order to adjust the band gap, one can manipulate the composition of the material through chemical doping or alloying. Theoretical and experimental studies have pointed out that these lattice defects from different types of atoms and doping sites are not only able to adjust the absorption edge but also able to modify in different ways the electronic structure and electronic conductivity of these materials: In the context of photocatalysis, transition metal (TM) doping of perovskite oxides is one of the most effective strategies to absorb visible light due to the  $3d$  bands of the dopant, which can cause a shift of the valence band and/or the conduction band and form new energy levels in the band gap [17–21].

Cations are in general implemented into the perovskite lattice by substitution with charge compensation in a number of

ways. According to the defect formation energies calculated in previous studies, TM elements are more likely favorable to replace the Ti site, leaving defects with an effective negative charge relative to the host lattice [18,22]. Recent studies of STO doped with several  $3d$  impurities have shown that Ni is one of the most promising dopants from the point of view of effective sunlight absorption [23]. In fact, the substitution of Ti atoms at the B site in STO with nickel (Ni), a divalent impurity with a  $d^8$  electronic configuration, compensated by oxygen vacancy reduces the band gap. The valency and chemical environment of Ni impurities in STO have been studied by many authors [23–29]. Some of the data indicated that Ni ions are present in the form of Ni<sup>2+</sup> in cubic sites and are substitutional on Ti<sup>4+</sup> sites [28], while others attested to the presence of features related to Ni<sup>3+</sup> with one oxygen vacancy [27] and even close to Ni<sup>4+</sup> [23]. The absorption edge shift of STO:Ni with respect to NiO was found to be 1.1 eV in Ref. [29] and 2.5 eV in Ref. [23]. Dissimilarity of the observed features was also present in the sample color. It was reported to be beige in Ref. [29] and black in Ref. [23].

Experimental data on the electronic structure of STO:Ni and the formation of Ni impurity bands are rare; yet several theoretical investigations from first-principles calculations are available [18,23,30]. Nevertheless, the availability of a variety of experimental and theoretical results made it difficult to undertake a direct comparison due to the use of different methods for sample preparation and associated characterization techniques [22,31,32].

In this paper, a detailed study of the electronic structure of STO(100) and STO:Ni<sub>x</sub>(100) thin films with  $x = 6$  and 12% deposited by pulsed laser deposition (PLD) is presented. The

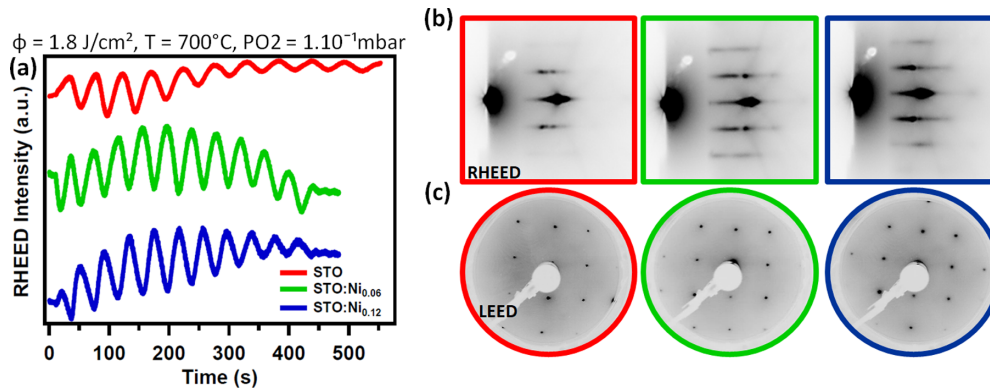


FIG. 1. Structural characterization of thin STO and STO:Ni<sub>x</sub> films grown on STO(100) substrate by PLD. (a) Intensity oscillations of the specular RHEED reflection. (b) Corresponding postgrowth RHEED patterns of the films. (c) LEED patterns of the undoped and Ni-doped STO films taken with an electron energy of 75 eV. All patterns exhibit a (1×1) reconstruction typical for the cubic perovskite (100) surface.

experimental results are compared with density functional theory (DFT) calculations based on the Korringa-Kohn-Rostoker (KKR) Green's function method [33,34].

## II. EXPERIMENTAL DETAILS

Pure STO and STO:Ni<sub>x</sub> thin films with Ni content of 6 and 12% were grown by PLD on STO substrates with an atomically flat (001) surface with the TiO<sub>2</sub> termination. In order to reduce charge effects during the photoemission measurements, the STO substrates were doped with 5% of Nb. Pressed powder targets, commercially available, with the desired stoichiometry were used (pure STO and STO:Ni<sub>x</sub> targets with  $x = 6$  and 12%). The substrate temperature during the growth was 700 °C, and oxygen pressure was  $1 \times 10^{-1}$  mbar. The thickness of the deposited films is about 4 nm, which is equivalent to 11 unit cells.

The PLD system is furthermore equipped with reflection high-energy electron diffraction (RHEED) and low-energy electron diffraction (LEED) setups to monitor the growth and the quality of films. An example of the RHEED intensity of the specular reflection during the growth process is shown in Fig. 1(a). The intensity oscillations indicate a layer-by-layer growth mode. There is, however, a qualitative difference between undoped and Ni-doped films. For the undoped STO films, the oscillations are initially strongly pronounced, and then they partially fade after depositing six unit cells ( $t = 300$  s). For the STO:Ni<sub>x</sub> films, the oscillations and their amplitudes are more intense and stable throughout the growth.

The postgrowth RHEED and LEED patterns are presented in Figs. 1(b) and 1(c), respectively. For the pure STO films, the diffraction patterns detected in RHEED are typical for a STO(100) surface as well as the pattern observed in LEED. The intensity and contrast of the RHEED patterns increase by increasing the Ni concentration in STO, suggesting that the STO:Ni<sub>x</sub> films are better ordered than STO films. The corresponding LEED patterns also show a (1×1) surface reconstruction similar to the STO(100) films; yet the diffraction signal appears to be of higher contrast for the doped samples.

After the growth, our samples were measured *in situ* by x-ray photoemission spectroscopy (XPS) with a monochromatic Al K<sub>α</sub> x-ray source of 1486.7 eV. X-ray absorption

(XAS), resonant photoemission (resPES), and angle-resolved photoemission spectroscopy (ARPES) measurements were performed at the PEARL and CASSIOPEE beamlines of the Swiss Light Source (SLS) and Synchrotron SOLEIL, respectively. For ARPES we used 200-eV linearly polarized photons, and the momentum and energy resolutions were 0.25° and 90 meV, respectively. Samples were transferred to the endstations in a vacuum suitcase ( $\sim 10^{-10}$  mbar) avoiding exposure to air. Our experiments were done in an ultrahigh-vacuum environment of  $\sim 10^{-10}$  mbar at room temperature, and the Fermi level was determined using a gold sample.

## III. COMPUTATIONAL DETAILS

All our calculations were performed within the framework of the Korringa-Kohn-Rostoker Green's function (KKR-GF) method based on multiple-scattering theory for the calculation of the electronic structure of materials [33,34]. The potential energy for the STO(100) bulk system with TiO<sub>2</sub> termination is induced in a self-consistent way using the atomic sphere approximation (ASA) together with the local density approximation (LDA). The impact of chemical disorder is handled by means of the coherent potential approximation (CPA) alloy theory [35,36], in which Ni atoms are randomly placed in substitution of Ti atoms and a new potential is generated. The lattice parameter used in this study is 3.905 Å. The  $l_{\max}$  value was fixed to 3 ( $f$  electrons) for the expansion in spherical harmonics. This will typically improve the calculated value for the band gap as compared with experimental values.

Our ARPES calculations are based on the so-called one-step model of photoemission [37], in which experimental parameters such as measurement geometry, photon energy, binding energy, and  $k$ -vector resolutions have been taken into account as input in this theoretical investigation.

## IV. RESULTS AND DISCUSSION

### Photoelectron spectroscopy measurements on STO(100) and STO:Ni(100) films

#### 1. XPS measurements

In order to identify the stoichiometry of the samples, and the chemical environment of Ni impurities, the core level

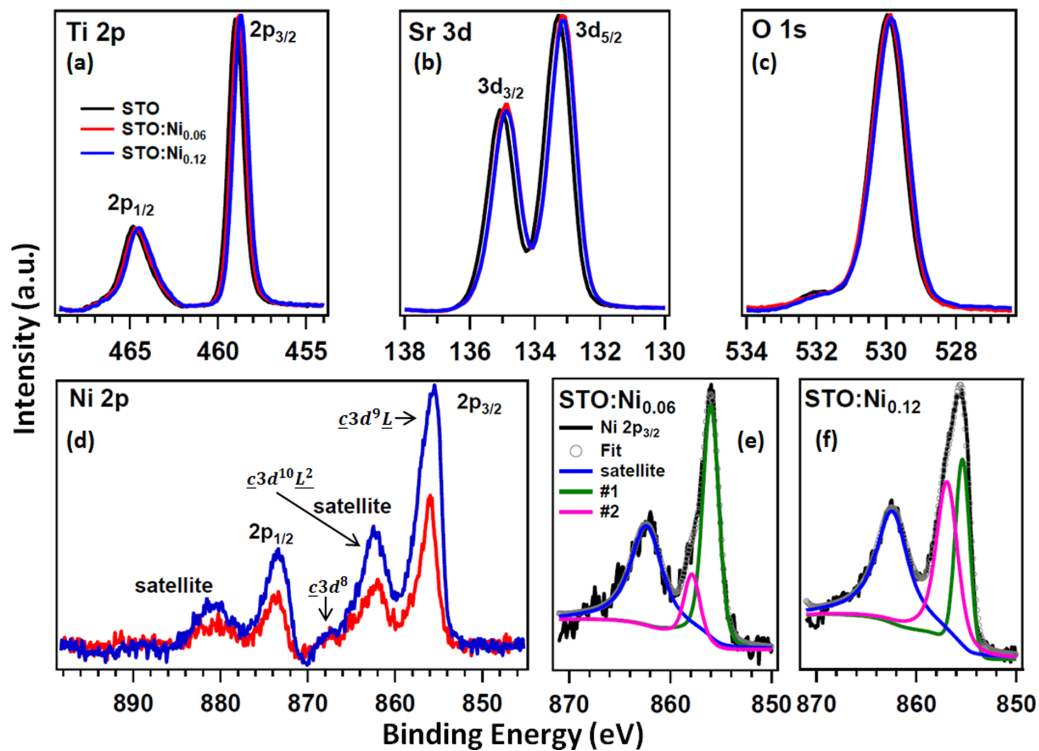


FIG. 2. (a)–(d) Core level intensity obtained with  $h\nu = 1486.6$  eV at normal emission for STO, STO:Ni<sub>0.06</sub>, and STO:Ni<sub>0.12</sub> films. All spectra are normalized by the Sr 3d spectral weight. (e) and (f) Ni 2p<sub>3/2</sub> spectra of STO:Ni<sub>0.06</sub> and STO:Ni<sub>0.12</sub> films, respectively. Voigt functions are used for fitting after Shirley background subtraction.

spectra for undoped and STO:Ni<sub>x</sub> films were measured by XPS, shown in Fig. 2. The XPS spectra of Sr 3d, Ti 2p, and O 1s in STO, STO:Ni<sub>0.06</sub>, and STO:Ni<sub>0.12</sub> films, displayed in Figs. 2(a)–(c), respectively, indicate that the individual spectral weights are independent of the presence of Ni. No detectable contamination by other elements, namely, carbon, is present.

A comparison of the Ni 2p spectra is presented in Fig. 2(d): In the case of STO:Ni<sub>0.06</sub> and STO:Ni<sub>0.12</sub>, the binding energy positions of the Ni 2p doublet are found at 855.6 eV (Ni 2p<sub>3/2</sub>) and 873.2 eV (Ni 2p<sub>1/2</sub>) separated by  $\Delta E = 17.6$  eV. In terms of orbital configuration, these peaks correspond to the Ni 2p final state  $\bar{c}3d^9L$ . At around 6 eV higher binding energy from each doublet line, satellite features are visible. They correspond to  $\bar{c}3d^8$  and  $\bar{c}3d^{10}L^2$  final states [38]. As expected, the spectral weight is increasing by a factor of 2 for the STO:Ni<sub>0.12</sub> sample in comparison to STO:Ni<sub>0.06</sub>.

The Ni 2p<sub>3/2</sub> spectra are fitted with Voigt functions as depicted in Figs. 2(e) and 2(f). For STO:Ni<sub>0.06</sub> films, fitting of the Ni 2p<sub>3/2</sub> line results in two components positioned at 855.8 and 857.7 eV ( $\Delta E = 1.9$  eV) labeled components 1 and 2, respectively. The first one is assigned to the oxidation state Ni<sup>2+</sup>, while the second component can have different explanations, which we are going to discuss further on. Similarly, for STO:Ni<sub>0.12</sub> films, two components of the Ni 2p<sub>3/2</sub> peak are fitted. The main Ni 2p line is positioned at 855.4 eV (component 1), and the second component (component 2) is positioned at 857 eV ( $\Delta E = 1.6$  eV). However, the spectral weight of the two components is not the same for the different samples. In the case of STO:Ni<sub>0.06</sub>, the intensity ratio of component 1 to component 2 is equal to 2.86, while in STO:Ni<sub>0.12</sub> the

contribution of component 2 increases significantly and the ratio decreases to 1.12.

For the interpretation of the extra component, component 2, located on the higher-binding-energy side of the main Ni 2p line we assume that Ni has an octahedral environment with oxygen ions in the films. The formation of component 2 results from a nonlocal screening process by an electron that does not come from the oxygen orbitals around the Ni atom with the core hole, but from a neighboring NiO<sub>6</sub> unit. Therefore we define component 1 as a locally screened core hole  $\bar{c}3d^9L$  and component 2 as a nonlocally screened core hole  $\bar{c}3d^9$ . Such an explanation was proposed previously to explain a similar structure of the Ni 2p XPS spectrum in NiO [39,40]. This hypothesis is verified by the difference seen in the spectral weight of component 2 as a function of Ni concentration in STO films, in which its contribution in STO:Ni<sub>0.06</sub> is relatively weak and becomes more important in STO:Ni<sub>0.12</sub>. According to our previous statement, this is expected for a Ni-rich environment, where the probability of having  $d^8L$  states available as next-nearest neighbors to a particular Ni ion, which provide the nonlocal screening, is much higher.

In addition to that, the component 2 peak might also have some surface state contribution resulting from pyramidally coordinated Ni atoms located at the surface of the films and overlaps with the nonlocal screening peak [41,42].

Angle-integrated XPS valence band (VB) spectra of undoped, STO:Ni<sub>0.06</sub>, and STO:Ni<sub>0.12</sub> films are displayed in Fig. 3(a<sub>1</sub>). All spectra are normalized to the maximum peak of the valence band located at 6 eV. The main features observed in all three spectra in the binding energy range between 3 and

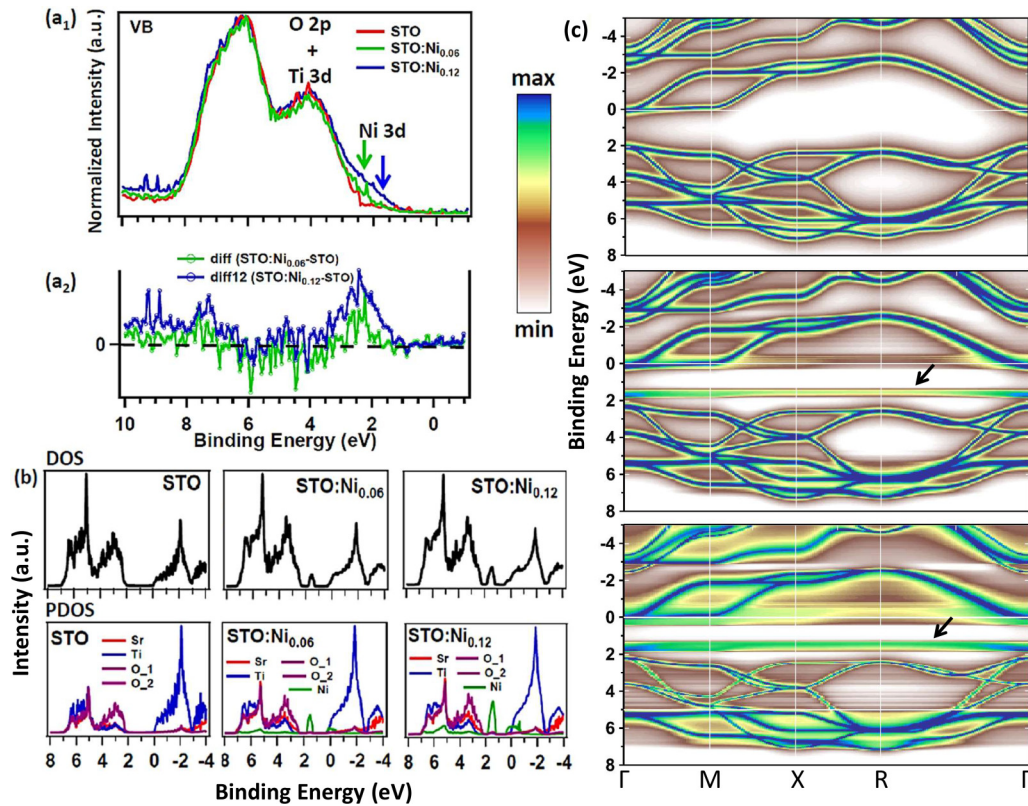


FIG. 3. (a<sub>1</sub>) Angle-integrated valence band of STO, STO:Ni<sub>0.06</sub>, and STO:Ni<sub>0.12</sub> recorded with monochromatic  $h\nu = 1486.6$  eV x rays directly after film growth (samples *in situ*). The spectra data are normalized to the maximum peak of the valence band located at 6 eV. The green and blue arrows assign the formation of in-gap states at the top of the valence band of the doped STO films at around 2–2.5 eV. (a<sub>2</sub>) A quantitative estimation of the new impurity states is given by subtracting the VB of the undoped films from the VB of the doped ones. *diff*, difference. (b) TDOS and PDOS for pure STO, STO:Ni<sub>0.06</sub>, and STO:Ni<sub>0.12</sub>. (c) Calculated ground-state band structures (Bloch spectral function) of the corresponding systems. Black arrows point to the Ni 3d levels in the band gap. The Fermi level is set to zero. The data are plotted using a logarithmic scale in order to enhance the intensity of the features related to the Ni 3d bands.

8 eV correspond to O 2*p* hybridized with Ti 3*d* states. For the doped samples, a formation of in-gap states located at the binding energy of 2–2.5 eV is indicated by the arrows.

A more quantitative view of these new states is obtained by subtracting the VB spectrum of the undoped film from the doped ones; see Fig. 3(a<sub>2</sub>). Clearly, their intensity is in line with the Ni content, indicating that this is a fingerprint of Ni 3*d* impurity levels in the STO gap.

In order to verify this assignment, in Fig. 3(b) we present calculated total (TDOSs) and partial densities of states (PDOSs) of Ni-doped STO and compare them with those of the undoped STO. Note that the calculated band-gap width in the undoped STO is 2 eV, which is lower than the experimental value. This is due to the shortcoming of DFT in describing the exchange-correlation potentials using the LDA. Here, we neglect the band-gap error for all systems, assuming that the relative change in the band gap of doped STO with respect to pure STO can provide the effect of Ni substitution.

The PDOS shows that the VB of pure STO is composed mostly of the O 2*p* states and the conduction band (CB) is dominated by Ti 3*d* states. For STO:Ni<sub>0.06</sub>, a wide distinct defect peak appears in the middle of the band gap, close to the VB maximum (VBM). As evidenced by the PDOS, it corresponds to Ni 3*d* states which are hybridized with O 2*p* states. The intensity of this peak increases by a factor of 2 in

STO:Ni<sub>0.12</sub>. A closer inspection of the PDOS unveils the Ni 3*d* contribution to the whole VB and as well to the CB edge.

The ground-state band structures of STO, STO:Ni<sub>0.06</sub>, and STO:Ni<sub>0.12</sub> are presented in Fig. 3(c). We used a logarithmic scale to plot the data in order to see better the Ni 3*d* localized bands in the gap as their intensity is relatively low compared with the bulk bands. In the undoped STO, which is our reference, the band-gap width at the  $\Gamma$  point is equal to 2 eV. For STO:Ni<sub>0.06</sub>, an atomlike flat defect band crosses the Brillouin zone resulting in a considerable reduction of the band-gap size. More precisely, the defect band is formed at 1.35 eV below the conduction band minimum (CBM). The intensity and width of the defect band increase by increasing the Ni-doping concentration in STO to 12%. In addition to the energy levels formed in the band gap of STO, new impurity states are also formed both in the CB and in the VB. Yet they do not participate in the modification of the band gap.

## 2. XAS and *resPES* measurements

We used *resPES* to investigate the correlated electronic structure of the 3*d* Ni states in STO. At energies close to the Ni L-edge absorption threshold, an interference between the direct photoemission channel and the dipole transition of a core electron to an unoccupied state (2*p* → 3*d*) occurs. This

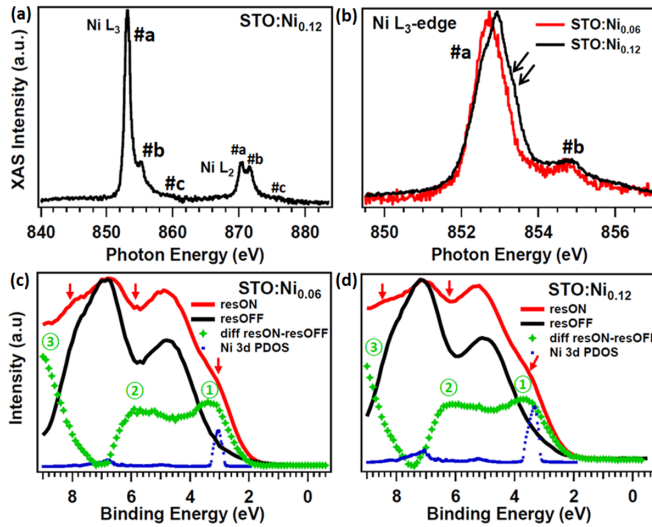


FIG. 4. (a) Ni  $L_{2,3}$  absorption spectra for STO:Ni $_{0.12}$ . (b) Comparison of the  $L_3$  absorption spectra for STO:Ni $_{0.06}$  and STO:Ni $_{0.12}$  films. Resonant photoemission measurements for the valence band of (c) STO:Ni $_{0.06}$  and (d) STO:Ni $_{0.12}$  films recorded with two photon energies: resON, photon energy around the Ni  $L_3$ -edge absorption ( $h\nu = 853.2$  eV); resOFF, photon energy below threshold ( $h\nu = 840$  eV). The difference between the valence bands' resON and resOFF and the Ni  $3d$  PDOS of STO:Ni systems are plotted. The Ni  $3d$  PDOS is manually shifted in binding energy to fit the experimental band gap of STO:Ni systems.

state decays in an Auger-like process. If the emitted Auger electron interferes coherently with the direct photoemission channel, it is resPES, giving rise to strong variations of the photoemission cross section [43–46].

Prior to resPES measurements we recorded  $L_{2,3}$ -edge XAS spectra from STO:Ni $_{0.06}$  and STO:Ni $_{0.12}$  films. We note that for both systems, the Ni XAS spectra have overall similar features; consequently, only the STO:Ni $_{0.12}$  spectrum is presented in Fig. 4(a). The main peaks of both  $L_3$  (853 eV) and  $L_2$  (870.2 eV) edges are labeled peak a. Two less intense features, lying at approximately 2 and 6 eV from the main peaks, are labeled peaks b and c, respectively. Peak b is due to multiplet splitting of the  $2p^53d^9$  state, resulting from the Coulomb interaction, exchange interaction, and crystal field effects, and peak c is attributed to a charge transfer excitation with configuration  $2p^53d^{10}\underline{L}$  [47].

A zoom on the  $L_3$  edge for STO:Ni $_{0.06}$  and STO:Ni $_{0.12}$  films is presented in Fig. 4(b). The main line (peak a) exhibits a broadening with increasing Ni concentration due to an additional feature, indicated by arrows on the higher-energy side. This broadening is likely to result from a nonlocal screening process that involves the Ni $^{2+}$  and the ligand states [39].

In order to determine the resonance enhancement of Ni  $3d$  related parts of the VB, spectra are taken at two photon energies: one at the maximum of the  $3d$  Ni absorption  $L$  edge (resON) and the second below threshold (resOFF). The difference (resON – resOFF) presented in Figs. 4(c) and 4(d) gives the resonance contribution, where we identified three major features labeled features 1, 2, and 3. The maxima of respective features lie at binding energies 3.5, 5.5, and 9 eV. The calculated Ni  $3d$  PDOS (blue dots) shows one main

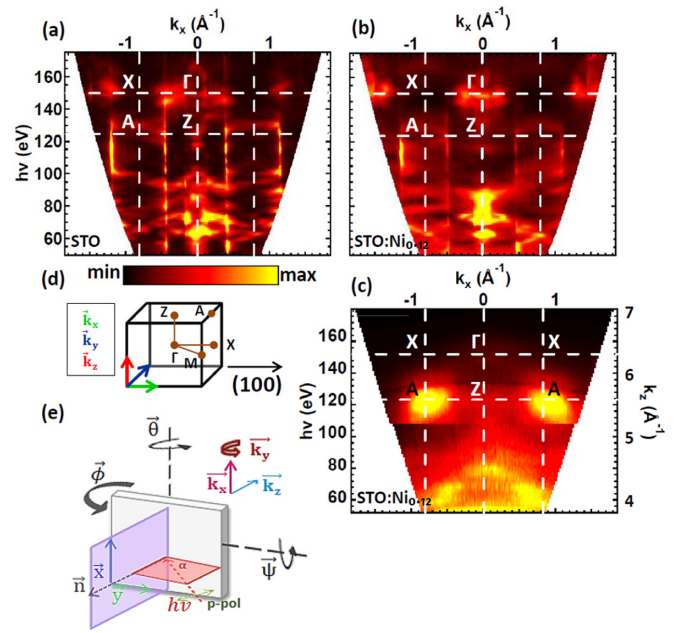


FIG. 5. (a) Dispersion with  $k_z$  at BE = 4 eV below the Fermi energy from  $h\nu = 50$  eV to  $h\nu = 175$  eV showing the high-symmetry points. The computational data from the one-step model of photoemission for bulk STO and STO:Ni $_{0.12}$  are displayed in (a) and (b), respectively. (c) Experimental data for STO:Ni $_{0.12}$  films. The data are plotted using a logarithmic scale. (d) First Brillouin zone of STO. (e) Measurement geometry.

peak that matches only with feature 1, leading us to assign it to a  $d^7$  final state configuration. Feature 2 is a resonance of the multiplet structure, reflecting the strongly correlated nature of Ni ions. Feature 3 is mainly related to an incoherent Auger decay not participating in the resonance photoemission process and resulting from the satellite located at 6 eV higher binding energy from Ni  $L_3$  [48–50].

We note that the LDA, used in our calculations, does not include correlation effects. Consequently, features 2 and 3, which involve correlations, cannot be obtained.

### 3. ARPES study

$k_z$ -dependent ARPES calculations for bulk STO(001) and STO:Ni $_{0.12}$ (001) together with the experimental data for STO:Ni $_{0.12}$ (001), all plotted at the binding energy (BE) of 4 eV, are shown in Figs. 5(a)–(c). The first Brillouin zone of STO and the experimental geometry are shown in Figs. 5(d) and 5(e). The conversion from  $h\nu$  to  $k_z$  is carried out within the free-electron final state approximation, with the inner potential of 14.65 eV retrieved from the periodicity observed in the measured spectra. The high-symmetry points at  $k_x = 0 \text{ \AA}^{-1}$ ,  $\Gamma$  and Z, and at  $k_x = 0.8 \text{ \AA}^{-1}$ , X and A, are labeled in Fig. 5(d).

At first glimpse, the main features in both bulk STO(001) and STO:Ni $_{0.12}$ (001) calculated spectra are very similar; see Figs. 5(a) and 5(b). The principal difference is the intensity embodied in the background all over the  $k_x$  and  $k_z$  ranges in the case of STO:Ni $_{0.12}$ . This intensity is purely related to the nondispersing Ni impurity bands formed at certain binding energy levels and confirms not only that these states are located around a specific symmetry point or direction but also

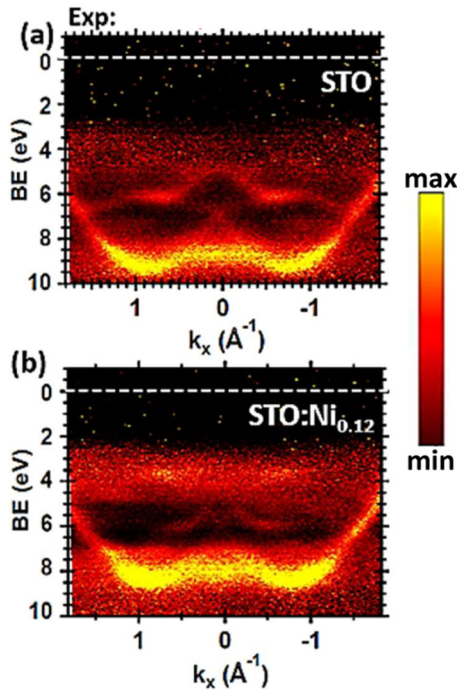


FIG. 6. Experimental band dispersion along the  $k_x$  direction for  $k_y = 0 \text{ \AA}^{-1}$  for (a) STO(001) and (b) STO:Ni<sub>0.12</sub>(001). The data show the bulk band dispersion and the localized impurity bands at the top of the valence band for the Ni-3d-doped STO films. All data are acquired with linearly polarized light of 200 eV. The measurements were performed at room temperature. The Fermi level is set to zero.

that they are homogeneously distributed in the whole volume of the Brillouin zone at a given binding energy. The other dissimilarities result from a slight upward binding energy shift of the bands for STO:Ni<sub>0.12</sub> compared with STO, as discussed in the next paragraph.

Note that in our calculations we used an extra-low imaginary part of the optical potential to resolve more features in the electronic band dispersion which can be hardly seen in our experiments due to lower energy resolution of the instruments, and results in a broadening of the bands. However, the main features observed in the experimental data displayed in Fig. 5(c) for STO:Ni<sub>0.12</sub>(001) films are in good agreement with the theoretical data: The  $\Gamma$  and  $Z$  points are detected at  $h\nu = 150$  and  $124$  eV, respectively, in the (100) direction. These values correspond to the third Brillouin zone along the  $k_z$  axis.

The experimental band dispersion for STO and STO:Ni<sub>0.12</sub> along the  $ZA$  direction is displayed in Fig. 6. All data are recorded with linearly polarized light of 200 eV for a wide binding energy range (10 eV below Fermi level). In the case of pure STO(001), the most significant feature is the dispersion of the O 2p bands partially hybridized with Ti 3d bands between 4.5 and 10 eV below the Fermi energy. In the case of Ni-doped STO films, the main bulk band between 7 and 9 eV is shifted to a lower binding energy level by 1 eV in comparison to pure STO films. The upper bands between 4 and 6 eV are shifted by 1.3 eV to lower binding energy. Back to the angle-integrated VBs measured by XPS in Fig. 3(a<sub>1</sub>), no binding energy shift of the bands between the undoped and

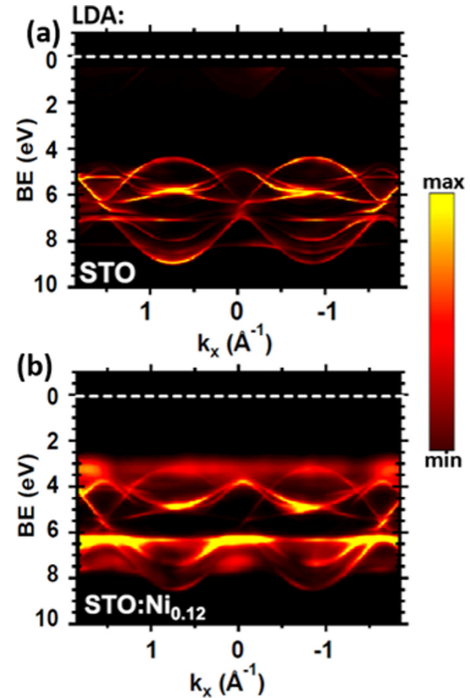


FIG. 7. ARPES calculations based on the one-step model of photoemission for (a) STO(001) and (b) STO:Ni<sub>0.12</sub>(001). The data show the bulk band dispersion and the localized impurity bands at the top of the valence band for the Ni-doped STO films. All data are acquired with linearly polarized light of 200 eV. The measurements were performed at room temperature. The Fermi level is set to zero.

doped STO is observed, in contrast to the data measured at 200 eV. In the latter case, the bands in STO are shifted to lower binding energies by approximately 500 meV compared with doped STO. We relate this shift to a band bending in pure STO, which induces an energy downshift of the O 2p VB creating a larger gap than the optical gap [8].

The corresponding ARPES calculations (one-step model of photoemission) are presented in Fig. 7. Here, a correction of the Fermi level position is applied so that it is compatible with the experimental value.

ARPES calculation for STO shows mainly the O 2p bands partially hybridized with Ti 3d bands [Fig. 7(a)]. The bandwidth is slightly underestimated compared with the experimental data, as well as their position with respect to the Fermi level. As already stressed, these disagreements reflect the limitations of DFT with LDA. Yet the calculated band dispersion of STO:Ni<sub>0.12</sub> reproduces quite well the measured one, notably the localized Ni 3d energy levels formed at the top of the VB [see Fig. 7(b)].

## V. CONCLUSIONS

In this paper, the electronic properties of STO doped with Ni are investigated. The samples were synthesized as thin films with thicknesses of a few nanometers using the PLD technique. A variety of spectroscopy techniques such as XPS, XAS, resPES, and ARPES were applied to achieve an understanding of the complicated many-body physics related to the Ni impurities, of atomlike

character, in STO films. In addition to experimental investigations, first-principles calculations within the KKR-GF method were performed.

In the case of STO:Ni(001) films, the analysis of the Ni  $2p$  core level spectra confirmed the presence of the oxidized form of the impurity atoms in STO and their location in an octahedral environment. From first-principles calculations for ground states and from the resPES measurements with photon energies around the  $3d$  Ni L edge, we could define the distribution of the  $3d$  impurity energy levels in the VB and CB and the band gap of STO. The localized defect bands in the band gap at the VBM will lead to an improvement in visible light absorption.

The Ni-resonant measurements revealed the strongly correlated nature of the Ni  $3d$  shell, where multiplet and satellite structures have an important contribution to the Ni L-edge resonance. The origin of these structures results mainly from strong Coulomb interaction, exchange interaction, and crystal field effects.

The ARPES data indicate that for the doped films, the bands are shifted towards the Fermi level, and the localized  $3d$  impurity bands were detected at 2.5 eV binding energy in the band gap of STO. One-step model calculations (LDA) reproduce nicely the band dispersion; however, we observe

discrepancies both in the Fermi level position and in the bandwidth. This can be explained by the fact that the calculations do not include all many-body effects and they underestimate the Coulomb potential.

## ACKNOWLEDGMENTS

This work was mainly supported by the CEDAMNF project, which is financed by the Ministry of Education, Youth and Sports of the Czech Republic, Project No. CZ.02.1.01/0.0/0.0/15.003/0000358. M.F. acknowledges support by Swiss National Science Foundation Project No. P2ELP2\_181877. The authors are also grateful for funding from the Deutsche Forschungsgemeinschaft (DFG, German Research Foundation) through the Würzburg-Dresden Cluster of Excellence on Complexity and Topology in Quantum Matter ct.qmat (EXC 2147, Project No. 390858490) as well as through the Collaborative Research Center SFB 1170 ToCoTronics (Project No. 258499086). This publication was published with the financial support of the European Union within the Project No. CZ.02.2.69/0.0/0.0/18\_054/0014627, Development of capacities and environment for boosting the international, intersectoral and interdisciplinary cooperation at UWB.

- 
- [1] N. Reyren, S. Thiel, A. D. Caviglia, L. F. Kourkoutis, G. Hammerl, C. Richter, C. W. Schneider, T. Kopp, A.-S. Ruetschi, D. Jaccard, M. Gabay, D. A. Muller, J.-M. Triscone, and J. Mannhart, Superconducting interfaces between insulating oxides, *Science* **317**, 1196 (2007).
- [2] K. Ueno, S. Nakamura, H. Shimotani, A. Ohtomo, N. Kimura, T. Nojima, H. Aoki, Y. Iwasa, and M. Kawasaki, Electric-field-induced superconductivity in an insulator, *Nat. Mater.* **7**, 855 (2008).
- [3] J. G. Bednorz and K. A. Müller, Perovskite-type oxides: The new approach to high- $T_c$  superconductivity, *Rev. Mod. Phys.* **60**, 585 (1988).
- [4] A. Brinkman, M. Huijben, M. van Zalk, J. Huijben, U. Zeitler, J. C. Maan, W. G. van der Wiel, G. Rijnders, D. H. A. Blank, and H. Hilgenkamp, Magnetic effects at the interface between non-magnetic oxides, *Nat. Mater.* **6**, 493 (2007).
- [5] T. Kimura, T. Goto, H. Shintani, K. Ishizaka, T. Arima, and Y. Tokura, Magnetic control of ferroelectric polarization, *Nature (London)* **426**, 55 (2003).
- [6] A. Ohtomo and H. Y. Hwang, A high-mobility electron gas at the  $\text{LaAlO}_3/\text{SrTiO}_3$  heterointerface, *Nature (London)* **427**, 423 (2004).
- [7] W. Meevasana, P. D. C. King, R. H. He, S.-K. Mo, M. Hashimoto, A. Tamai, P. Songsirittigul, F. Baumberger, and Z.-X. Shen, Creation and control of a two-dimensional electron liquid at the bare  $\text{SrTiO}_3$  surface, *Nat. Mater.* **10**, 114 (2011).
- [8] A. F. Santander-Syro, O. Copie, T. Kondo, F. Fortuna, S. Pailhès, R. Weht, X. G. Qiu, F. Bertran, A. Nicolaou, A. Taleb-Ibrahimi, P. L. Fèvre, G. Herranz, M. Bibes, N. Reyren, Y. Apert, P. Lecoeur, A. Barthélémy, and M. J. Rozenberg, Two-dimensional electron gas with universal subbands at the surface of  $\text{SrTiO}_3$ , *Nature (London)* **469**, 189 (2011).
- [9] Z. Wang, S. M. Walker, A. Tamai, Y. Wang, Z. Ristic, F. Y. Bruno, A. de la Torre, S. Riccò, N. C. Plumb, M. Shi, P. Hlawenka, J. Sánchez-Barriga, A. Varykhalov, T. K. Kim, M. Hoesch, P. D. C. King, W. Meevasana, U. Diebold, J. Mesot, B. Moritz *et al.*, Tailoring the nature and strength of electron-phonon interactions in the  $\text{SrTiO}_3(001)$  2D electron-liquid, *Nat. Mater.* **15**, 835 (2016).
- [10] Y. Okamoto, R. Fukui, M. Fukazawa, and Y. Suzuki,  $\text{SrTiO}_3/\text{TiO}_2$  composite electron transport layer for perovskite solar cells, *Mater. Lett.* **187**, 111 (2017).
- [11] P. Jayabal, V. Sasirekha, J. Mayandi, K. Jeganathan, and V. Ramakrishnan, A facile hydrothermal synthesis of  $\text{SrTiO}_3$  for dye sensitized solar cell application, *J. Alloys Compd.* **586**, 456 (2014).
- [12] Z. G. Sheng, M. Nakamura, W. Koshibae, T. Makino, Y. Tokura, and M. Kawasaki, Magneto-tunable photocurrent in manganite-based heterojunctions, *Nat. Commun.* **5**, 4584 (2014).
- [13] S. Wu, X. Gao, M. Qin, J.-M. Liu, and S. Hu,  $\text{SrTiO}_3$  modified  $\text{TiO}_2$  electrodes and improved dye-sensitized  $\text{TiO}_2$  solar cells, *Appl. Phys. Lett.* **99**, 042106 (2011).
- [14] S. Yang, H. Kou, H. Wang, K. Cheng, and J. Wang, The photoelectrochemical properties of  $\text{N}_3$  sensitized  $\text{CaTiO}_3$  modified  $\text{TiO}_2$  nanocrystalline electrodes, *Electrochim. Acta* **55**, 305 (2009).
- [15] L. Zhang, Y. Shi, S. Peng, J. Liang, Z. Tao, and J. Chen, Dye-sensitized solar cells made from  $\text{BaTiO}_3$ -coated  $\text{TiO}_2$  nanoporous electrodes, *J. Photochem. Photobiol., A* **197**, 260 (2008).
- [16] K. van Benthem, C. Elssser, and R. H. French, Bulk electronic structure of  $\text{SrTiO}_3$ : Experiment and theory, *J. Appl. Phys. (Melville, NY)* **90**, 6156 (2001).

- [17] J. Liu, G. Chen, Z. Li, and Z. Zhang, Electronic structure and visible light photocatalysis water splitting property of chromium-doped SrTiO<sub>3</sub>, *J. Solid State Chem.* **179**, 3704 (2006).
- [18] F. Li, K. Yu, L.-L. Lou, Z. Su, and S. Liu, Theoretical and experimental study of La/Ni co-doped SrTiO<sub>3</sub> photocatalyst, *Mater. Sci. Eng., B* **172**, 136 (2010).
- [19] R. Niishiro, H. Kato, and A. Kudo, Nickel and either tantalum or niobium-codoped TiO<sub>2</sub> and SrTiO<sub>3</sub> photocatalysts with visible-light response for H<sub>2</sub> or O<sub>2</sub> evolution from aqueous solutions, *Phys. Chem. Chem. Phys.* **7**, 2241 (2005).
- [20] H.-C. Chen, C.-W. Huang, J. C. S. Wu, and S.-T. Lin, Theoretical investigation of the metal-doped SrTiO<sub>3</sub> photocatalysts for water splitting, *J. Phys. Chem. C* **116**, 7897 (2012).
- [21] X. Zhou, J. Shi, and C. Li, Effect of metal doping on electronic structure and visible light absorption of SrTiO<sub>3</sub> and NaTaO<sub>3</sub> (metal = Mn, Fe, and Co), *J. Phys. Chem. C* **115**, 8305 (2011).
- [22] X.-L. Dong, K.-H. Zhang, and M.-X. Xu, First-principles study of electronic structure and magnetic properties of SrTi<sub>1-x</sub>M<sub>x</sub>O<sub>3</sub> (M = Cr, Mn, Fe, Co, or Ni), *Front. Phys.* **13**, 137106 (2018).
- [23] I. A. Sluchinskaya, A. I. Lebedev, and A. Erko, Structural position and charge state of nickel in SrTiO<sub>3</sub>, *Phys. Solid State* **56**, 449 (2014).
- [24] K. Blazey and H. Weibel, Optical absorption spectra of reduced transition-metal ion-doped SrTiO<sub>3</sub>, *J. Phys. Chem. Solids* **45**, 917 (1984).
- [25] S. K. Rout, S. Panigrahi, and J. Bera, Study on electrical properties of Ni-doped SrTiO<sub>3</sub> ceramics using impedance spectroscopy, *Bull. Mater. Sci.* **28**, 275 (2005).
- [26] P. Koidl, K. W. Blazey, W. Berlinger, and K. A. Miller, Photochromism in Ni-doped SrTiO<sub>3</sub>, *Phys. Rev. B* **14**, 2703 (1976).
- [27] K. A. Miller, W. Berlinger, and R. S. Rubins, Observation of two charged states of a nickel-oxygen vacancy pair in SrTiO<sub>3</sub> by paramagnetic resonance, *Phys. Rev.* **186**, 361 (1969).
- [28] B. W. Faughnan, Photochromism in transition-metal-doped SrTiO<sub>3</sub>, *Phys. Rev. B* **4**, 3623 (1971).
- [29] A. M. Beale, M. Paul, G. Sankar, R. J. Oldman, C. R. A. Catlow, S. French, and M. Fowles, Combined experimental and computational modelling studies of the solubility of nickel in strontium titanate, *J. Mater. Chem.* **19**, 4391 (2009).
- [30] A. I. Lebedev and I. A. Sluchinskaya, On the nature of change in Ni oxidation state in BaTiO<sub>3</sub> and SrTiO<sub>3</sub> system, *Ferroelectrics* **501**, 1 (2016).
- [31] S. S. Ghosh and E. Manousakis, Structure and ferromagnetic instability of the oxygen-deficient SrTiO<sub>3</sub> surface, *Phys. Rev. B* **94**, 085141 (2016).
- [32] S. Gerhold, M. Riva, Z. Wang, R. Bliem, M. Wagner, J. Osiecki, K. Schulte, M. Schmid, and U. Diebold, Nickel-oxide-modified SrTiO<sub>3</sub>(110)-(4×1) surfaces and their interaction with water, *J. Phys. Chem. C* **119**, 20481 (2015).
- [33] J. Braun, The theory of angle-resolved ultraviolet photoemission and its applications to ordered materials, *Rep. Prog. Phys.* **59**, 1267 (1996).
- [34] H. Ebert, D. Kdderitzsch, and J. Minár, Calculating condensed matter properties using the KKR-Green's function method—recent developments and applications, *Rep. Prog. Phys.* **74**, 096501 (2011).
- [35] J. Faulkner, The modern theory of alloys, *Prog. Mater. Sci.* **27**, 1 (1982).
- [36] P. Soven, Coherent-potential model of substitutional disordered alloys, *Phys. Rev.* **156**, 809 (1967).
- [37] J. Braun, J. Minár, and H. Ebert, Correlation, temperature and disorder: Recent developments in the one-step description of angle-resolved photoemission, *Phys. Rep.* **740**, 1 (2018).
- [38] S. Hüfner, Electronic structure of NiO and related 3d-transition-metal compounds, *Adv. Phys.* **43**, 183 (1994).
- [39] H. Stefan, *Photoelectron Spectroscopy: Principles and Applications* (Springer, New York, 2003).
- [40] M. A. van Veenendaal and G. A. Sawatzky, Nonlocal Screening Effects in 2p X-Ray Photoemission Spectroscopy Core-Level Line Shapes of Transition Metal Compounds, *Phys. Rev. Lett.* **70**, 2459 (1993).
- [41] I. Preda, A. Gutiérrez, M. Abbate, F. Yubero, J. Méndez, L. Alvarez, and L. Soriano, Interface effects in the Ni 2p x-ray photoelectron spectra of NiO thin films grown on oxide substrates, *Phys. Rev. B* **77**, 075411 (2008).
- [42] L. Soriano, I. Preda, A. Gutiérrez, S. Palacín, M. Abbate, and A. Vollmer, Surface effects in the Ni 2p x-ray photoemission spectra of NiO, *Phys. Rev. B* **75**, 233417 (2007).
- [43] U. Fano, Effects of configuration interaction on intensities and phase shifts, *Phys. Rev.* **124**, 1866 (1961).
- [44] Y. Sakisaka, T. Komeda, M. Onchi, H. Kato, S. Masuda, and K. Yagi, Photoemission study of the valence-band satellite of Ni(110), *Phys. Rev. B* **36**, 6383 (1987).
- [45] A. Liebsch, Effect of Self-Energy Corrections on the Valence-Band Photoemission Spectra of Ni, *Phys. Rev. Lett.* **43**, 1431 (1979).
- [46] G. van der Laan, B. T. Thole, H. Ogasawara, Y. Seino, and A. Kotani, Strong resonances in core-level photoemission, *Phys. Rev. B* **46**, 7221 (1992).
- [47] G. van der Laan, J. Zaanen, G. A. Sawatzky, R. Karnatak, and J.-M. Esteve, Comparison of x-ray absorption with x-ray photoemission of nickel dihalides and NiO, *Phys. Rev. B* **33**, 4253 (1986).
- [48] M. Weinelt, A. Nilsson, M. Magnuson, T. Wiell, N. Wassdahl, O. Karis, A. Föhlisch, N. Mårtensson, J. Stöhr, and M. Samant, Resonant Photoemission at the 2p Edges of Ni: Resonant Raman and Interference Effects, *Phys. Rev. Lett.* **78**, 967 (1997).
- [49] N. Mårtensson, M. Weinelt, O. Karis, M. Magnuson, N. Wassdahl, A. Nilsson, J. Stöhr, and M. Samant, Coherent and incoherent processes in resonant photoemission, *Appl. Phys. A: Mater. Sci. Process.* **65**, 159 (1997).
- [50] M. López, C. Laubschat, A. Gutiérrez, E. Weschke, A. Höhr, M. Domke, and G. Kaindl, Coherence versus incoherence of photoemission and Auger signals at resonance, *Surf. Sci.* **307-309**, 907 (1994).